Wideband Steady-State Model of a Strained InGaAsP MQW-SOA

Michael J. Connelly, *Senior Member, IEEE*, Simone Mazzucato, Hélène Carrere, Xavier Marie, Thierry Amand, Mohand Achouche, Christophe Caillaud, and Romain Brenot

***Abstract*—A steady-state model of a strained MQW-SOA is described. Least-squares fitting of the model to experimental polarization resolved amplified spontaneous emission spectra is used to obtain difficult to measure model parameters such as the linebroadening lineshape parameters, Auger recombination, bandgap shrinkage, and intervalence band absorption coefficients. Well capture and escape processes are modeled by a carrier density dependent net escape time which accounts for barrier effects. Simulations and comparisons with experimental data are given which demonstrate the accuracy and versatility of the model.**

***Index Terms*—Modeling, quantum wells, semiconductor optical amplifier.**

I. Introduction

THE rapid expansion of optical networks requires the availability of small, inexpensive and easy to integrate optical amplifiers. InP-based semiconductor optical amplifiers (SOAs) with InGaAsP/InGaAsP multi-quantum-well (MQW) active regions are good candidates for 10 Gb/s coarse WDM communications. These devices should provide a wide optical bandwidth and be polarization insensitive. InGaAsP quaternary multi-QWs have already been investigated for SOA applications. Polarization insensitive operation can be obtained by stacking tensile and compressive QWs in the active layer [1]. Compressive-strained QWs have predominantly TE gain, while tensile-strained QWs have predominantly TM gain. In [2] it was shown that active material gain coefficient polarization independence ($<$1 dB TE/TM gain coefficient difference) can be achieved along with a wide optical bandwidth, by using one-width MQWs. The measured amplified emission spectrum however had relatively high polarization sensitivity. It is necessary to develop a device model that can be used to aid in its optimization especially with regard to improving polarization sensitivity. In this paper we describe such a steady-state model, which uses full bandstructure calculations to obtain the TE, TM gain coefficients and spontaneous recombination rate. The amplified signal and Amplified Spontaneous Emission (ASE) are described by travelling-wave equations that are solved along with a carrier density rate equation. Unknown model parameters are obtained by using least-squares fitting of the model to the measured output ASE spectra for a range of bias currents.

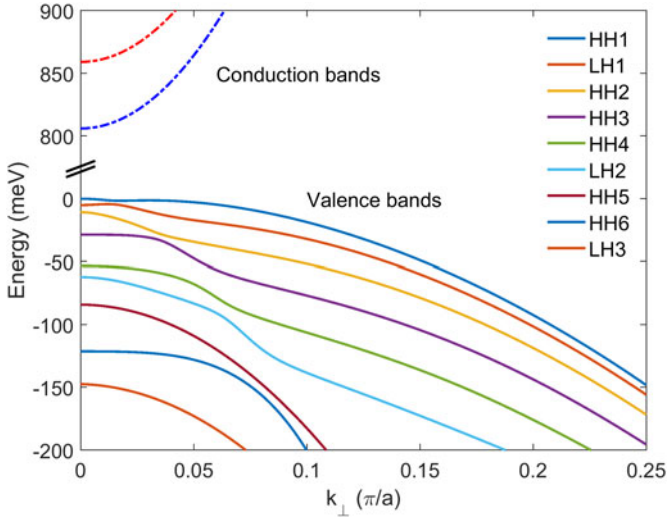

Fig. 1. QW bandstructure, with Heavy Hole (HH) and Light Hole (LH) valence bands indicated. All confined levels are taken into account in the material gain calculations.

II. SOA Geometry, Bandstructure and Material Gain

The investigated SOA active region consists of three 14 nm thick $In_{0.53}Ga_{0.47}As_{0.96}P_{0.04}$ QWs with 15 nm $In_{0.8}Ga_{0.2}As_{0.45}P_{0.55}$ barriers made of Q1.17 material as is the 100 nm wide separate confinement heterostructure layer, as described in [2]. The conduction band, valence band heavy hole and light hole offsets for these alloys are 113, 159 and 173 meV respectively. Carrier overflow towards the barrier is taken into account but probably underestimated as our calculations were made for 300 K operation. Drift and diffusion transport effects are not considered in the model.

The SOA length L and active stripe width W are 2 mm and 1.75 μm respectively. The QW bandstructure, shown in Fig. 1, was calculated by solving the Lüttinger–Kohn Hamiltonian, including tetragonal strain, confinement effects and taking into account the interfacial discontinuity condition [3]–[6]. According to the barrier height, two conduction and nine valence energy bands are confined to the QWs.

Manuscript received July 13, 2015; revised March 18, 2016 and December 16, 2015; accepted March 30, 2016. Date of publication April 3, 2016; date of current version April 30, 2016. This work was supported by the Jasmin Project N°ANR-11-INFR-007 and Science Foundation Ireland Investigator under Grant 09/IN.1/I2641.

M. J. Connelly is with the Optical Communications Research Group, Department of Electronic and Computer Engineering, University of Limerick, Limerick V94 T9PX, Ireland (e-mail: michael.connelly@ ul.ie).

S. Mazzucato, H. Carrere, X. Marie, and T. Amand are with the INSA, UPS, LPCNO, Université de Toulouse, Toulouse F-31077, France (e-mail: mazzucat@insa-toulouse.fr).

M. Achouche, C. Caillaud and R. Brenot are with the Alcatel Thales III-V Lab, Cedex F- 91767, France (e-mail: mohand.achouche@3-5lab.fr; christophe.caillaud@3-5lab.fr; romain.brenot@3-5lab.fr).

Color versions of one or more of the figures in this paper are available online at http://ieeexplore.ieee.org.

Digital Object Identifier 10.1109/JLT.2016.2550183

The active region bandgap, including carrier shrinkage due to the well carrier density n, is given by

$$E_g = E_{g0} - K_g n^{1/3} \tag{1}$$

where $E_{g0} = 806$ meV. The bandgap shrinkage coefficient K_g is considered to be a fitting parameter. The energy E dependent spontaneous emission rate $r_{\rm sp}$ and material gain g_m per well are given by [7], [8],

$$r_{\rm sp}^{\rm TE/TM}(E) = \frac{4n_r e^2 E}{\pi m_0^2 \varepsilon_0 h^2 c^3 L_w} \sum_i \sum_j \int_0^\infty k_\perp |M_{\rm ij}^{\rm TE/TM}(k_\perp)|^2 \times f_c(E_i(k_\perp))[1 - f_v(E_j(k_\perp)]L(E_{\rm ij}(k_\perp))dk_\perp \tag{2}$$

$$g_m^{\rm TE/TM}(E) = \frac{e^2\hbar}{\pi m_0^2 \varepsilon_0 n_r c L_w E}\left[1 - \exp\left(\frac{E - \Delta E_F}{k_B T}\right)\right] \times \sum_i \sum_j \int_0^\infty k_\perp |M_{\rm ij}^{\rm TE/TM}(k_\perp)|^2 f_c(E_i(k_\perp)) \times [1 - f_v(E_j(k_\perp)]L(E_{\rm ij}(k_\perp))dk_\perp \tag{3}$$

m_0 is the electron mass, ε_0 the permittivity of free-space, $k_\perp$ the momentum, $M_{\rm ij}^{\rm TE/TM}(k_\perp)$ the matrix elements, E_i and E_j the ith and jth conduction and valence bands respectively, $E_{\rm ij}$ the associated transition energies, f_c and f_v the conduction band and valence band Fermi–Dirac functions respectively, ΔE_F the quasi-Fermi level difference, L_w the well width, n_r the material refractive index, k_B the Boltzmann constant. The temperature T is taken to be 300 K. $r_{\rm sp}$ can be written as

$$r_{\rm sp}^{\rm TE/TM}(E) = \frac{8\pi n_r^2 E^2}{h^3 c^2} \times \left[1 - \exp\left(\frac{E - \Delta E_F}{k_B T}\right)\right]^{-1} g_m^{\rm TE/TM}(E) \tag{4}$$

so

$$g_m^{\rm TE/TM}(E) = \left[1 - \exp\left(\frac{E - \Delta E_F}{k_B T}\right)\right] g_{\rm sp}^{\rm TE/TM}(E) \tag{5}$$

with

$$g_{\rm sp}^{\rm TE/TM}(E) = \frac{h^3 c^2}{8\pi n_r^2 E^2} r_{\rm sp}^{\rm TE/TM}(E) \tag{6}$$

$g_{\rm sp}$ has the same dimensions as the material gain. The choice of lineshape function has a critical impact on the shape of the material gain spectrum. $L(E)$ is a broadening function used to account for intraband relaxation and other broadening effects. A common choice of lineshape is a Lorentzian; however in reality the actual lineshape is asymmetric, with a sharper tail on the high energy side of its peak. We use an asymmetric Lorentzian lineshape [9],

$$L(E) = K \frac{E_{\rm int}\left[1 + \exp\left(E/E_{\rm asy}\right)\right]^{-1}}{E^2 + E_{\rm int}^2\left[1 + \exp\left(E/E_{\rm asy}\right)\right]^{-2}} \tag{7}$$

$E_{\rm int}$ is the Lorentzian Full Width at Half Maximum (FWHM) when the asymmetry energy parameter $E_{\rm asy}$ is infinite, in which case (7) is a symmetrical Lorentzian. Negative values of $E_{\rm asy}$ skew the lineshape toward higher energies while positive values skew it toward lower energies. K is a normalization constant such that the integral of $L(E)$ overall energies is equal to 1. This lineshape function is a good analytical approximation to that obtained from detailed theoretical calculations for quantum-wells where the principle linebroadening mechanisms are hole-hole, electron-hole and longitudinal optical phonon scattering [10]. The determination of the exact broadening profile requires the many-body treatment for electron-hole plasma which is out of the scope of this study. The form of the lineshape is shown in Fig. 2 using the model extracted parameters.

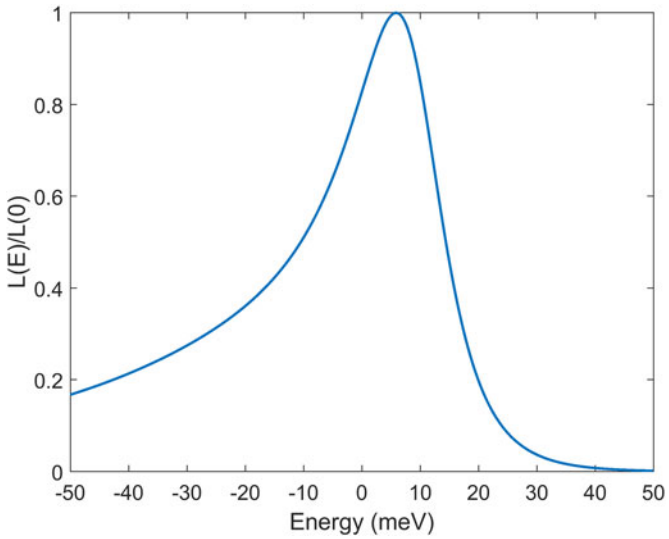

Fig. 2. Normalized asymmetric Lorentzian lineshape with $E_{\rm int} = 41$ meV and $E_{\rm asy} = 10.0$ meV. The FWHM is 24.4 meV.

The conduction band quasi-Fermi level $E_{\rm fc}$ is obtained by numerically solving the charge neutrality equation

$$n = \frac{\pi}{a^2 L_w} \sum_i \int_0^\infty \frac{k_\perp}{1 + \exp\left\{\left[E_i(k_\perp) - E_{\rm fc}\right]/k_B T\right\}} dk_\perp \tag{8}$$

where $a = 0.586$ nm is the lattice constant. A similar equation is used to determine the valence band quasi-Fermi level, where it is assumed that the hole and electron densities are equal. The dependency of the quasi-Fermi levels on carrier density are shown in Fig. 3. Typical spectral plots of g_m and $g_{\rm sp}$ are shown in Fig. 4, for TE and TM transition modes, calculated at different injection carrier densities.

The net gain coefficient is modeled by

$$g^{\rm TE/TM} = N_w \Gamma_{\rm TE/TM} g_m^{\rm TE/TM} - \alpha \tag{9}$$

$\Gamma_{\rm TE/TM}$ is the polarization dependent optical confinement factor per well. The TE and TM confinement factors per well are 1.97% and 1.42% respectively calculated using the Fimmwave mode solver. N_w is the number of QWs. The polarization dependent loss coefficient is modeled as

$$\alpha = \alpha_0 + N_w \Gamma_{\rm TE/TM} \alpha_{1,\rm TE/TM} n \tag{10}$$

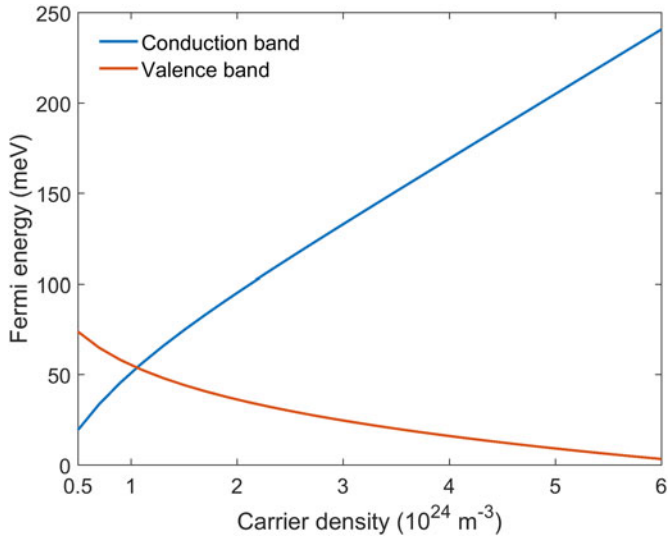

Fig. 3. Carrier density dependence of the quasi-Fermi levels relative to the band edge.

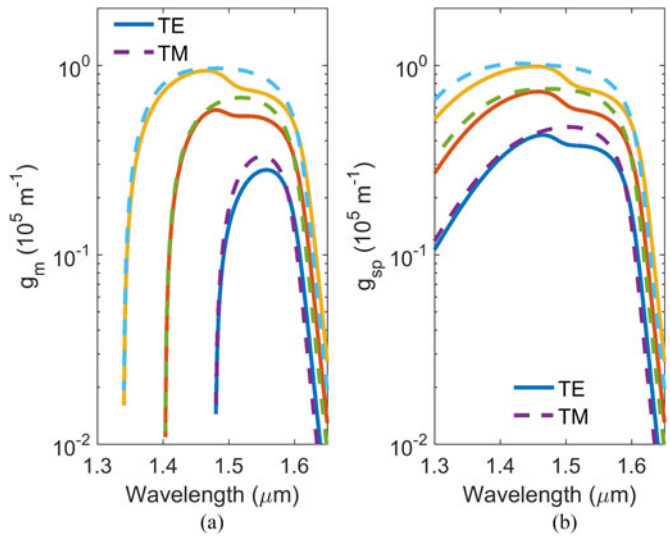

Fig. 4. (a) g_m and (b) $g_{\rm sp}$ coefficients per well for carrier densities of 2, 3 and 4 $\times$ 10^{24} m^{-3}. The higher curves correspond to increasing carrier density.

where α_0 is the intrinsic material and $\alpha_{1,\rm TE/TM}$ the polarization dependent InterValence Band Absorption (IVBA) loss coefficients [12], [13]. These are also treated as fitting parameters.

III. Model and Experiment

For a given carrier density spatial distribution in the SOA the signal photon rate N_s at a distance z from the SOA input is given by

$$N_s(z) = \frac{P_{\rm in}}{E_s} \exp\left(\int_0^z g_s dz\right) \tag{11}$$

where g_s is the net gain coefficient at the signal energy E_s and polarization and $P_{\rm in}$ is the input optical power. The forward and backward travelling ASE photon rates $N^{\pm}_{\rm TE/TM,k}$ in the kth spectral slice of energy width ΔE centered at energy E_k are obtained from finite difference solutions to the traveling-wave equations [11],

$$\frac{dN^{\pm}_{\rm TE/TM,k}}{dz} = \pm g_k^{\rm TE/TM} N^{\pm}_{\rm TE/TM,k} \pm N_w \Gamma_{\rm TE/TM} g_{{\rm sp},k}^{\rm TE/TM} \Delta E/h \tag{12}$$

where g_k is the net gain coefficient at E_k. The polarization resolved output ASE power at wavelength λ_k (corresponding to E_k) in a wavelength resolution bandwidth $\Delta\lambda_{\rm res}$ is given by

$$P_{\rm TE/TM,k} = N^{+}_{\rm TE/TM,k}(z=L)\frac{h^2c^2\Delta\lambda_{\rm res}}{\lambda_k^3 \Delta E}. \tag{13}$$

The well carrier density n rate equation, assuming no spontaneous carrier recombination in the barrier regions and ignoring diffusion effects, is given by

$$\frac{dn}{dt} = \frac{I}{eN_wL_wWL} - R(n) - \frac{\Gamma_{\rm TE/TM} n_w g_m}{L_w W} N_s - \frac{N_w}{L_w W} \sum_{i={\rm TE,TM}} \sum_k \Gamma_i(z) g^i_{m,k} [N^+_{i,k} + N^-_{i,k}]. \tag{14}$$

The first term on the right hand side of (14) is the electrical pumping due to the bias current *I* assuming that all the injected carriers enter the QWs and that there is negligible radiative recombination in the barrier regions. The recombination rate $R(n)$ is modeled as

$$R(n) = \frac{n}{\tau_{\rm esc}} + R_{\rm rad}(n) + Cn^3. \tag{15}$$

The net carrier escape/capture processes from and to the QWs are modeled by the first term in $R(n)$, in which the net escape time $\tau_{\rm esc}$ from each QW is assumed to depend on the carrier density as,

$$\tau_{\rm esc} = \frac{\tau_{\rm esc0}}{1 + e^{p(n-n_0)}} \tag{16}$$

where n_0 is the carrier density for which the quasi-Fermi level of the confined electrons equals the barrier height and p is an abruptness parameter that determines how quickly the escape time decreases from its low carrier density value $\tau_{\rm esc0}$ [14]. These parameters are considered to be fitting parameters. The Auger recombination coefficient C is also considered to be a fitting parameter. The total spontaneous radiative recombination rate per well $R_{\rm rad}$ is calculated as

$$R_{\rm rad} = \int_0^\infty r_{\rm sp} dE = \frac{8\pi n_r^2}{h^3c^2} \int_0^\infty (g_{\rm sp,TE} + g_{\rm sp,TM}) E^2 dE. \tag{17}$$

The carrier density dependence of $R_{\rm rad}$ on carrier density is shown in Fig. 5. $R_{\rm rad}$ is often assumed to be a bimolecular recombination process approximated by $R_{\rm rad} \approx Bn^2$, where B is the bimolecular recombination coefficient; however as Fig. 5 shows, this is not particularly accurate for this device.

The SOA model equations cannot be solved analytically, so a numerical solution is required. The algorithm used is essentially

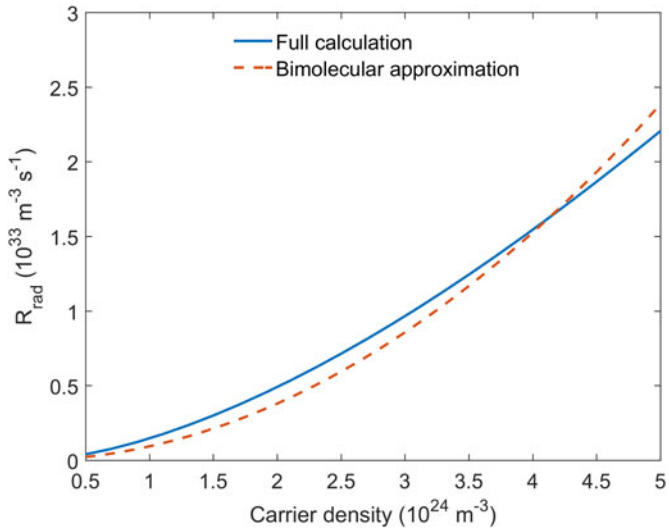

Fig. 5. Spontaneous radiative recombination rate per well versus carrier density and bimolecular approximation.

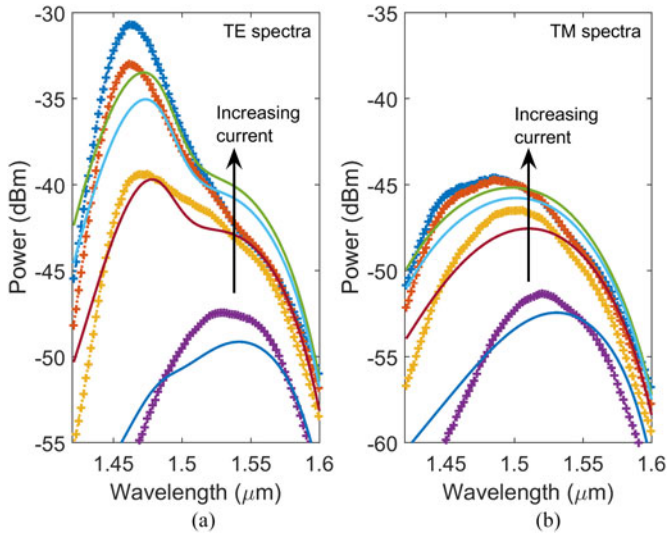

Fig. 6. Experimental (+) and simulated (−): (a) TE and (b) TM output ASE spectra for bias currents of 100, 200, 300 and 400 mA. The resolution bandwidth is 0.1 nm.

similar to that described in [11]–[15]. The SOA is split into 128 spatial sections and the ASE into 1024 spectral slices covering a range of 1250 to 1650 nm. Initially the carrier density in the amplifier is set to some reasonable value (2×10^{24} m^{-3}). The signal intensity and ASE photon rates are then estimated at the section interfaces using finite difference solutions to (10) and (11). The carrier density is then estimated at the center of each section (using (14) with the time derivative set to zero), which is then used to update the material gain and spontaneous emission coefficients and subsequently the signal and ASE. This process is continued until the values of the ASE photon rates converge to a tolerance of less than 0.1%. The unknown model parameters were obtained using Levenberg–Marquardt least-squares fitting of the output ASE spectra to model predictions

TABLE I
EXTRACTED PARAMETERS

$E_{\rm int}$	41 meV
$E_{\rm asy}$	10 meV
$\tau_{\rm esc0}$	2.7 ns
p	9.3×10^{-24} m^3
n_0	3.2×10^{24} m^{-3}
K_g	1.1×10^{-10} eVm
C	2.3×10^{-40} m$^6 \cdot$ s^{-1}
α_0	1330 m^{-1}
$\alpha_{1,TE}$	0.57×10^{-20} m^2
$\alpha_{1,TM}$	1.19×10^{-20} m^2

for bias currents of 100, 200, 300 and 400 mA as shown in Fig. 6.

The extracted parameters are shown in Table I. The RMS error between experiment and simulations for TE and TM ASE spectra is 1.9 and 1.2 dB respectively. The match between the model and simulation is good for the TM spectra, but somewhat less so for TE. IVBA increases with energy so including this dependency could possibly improve the matching; however this would involve more fitting parameters [12]. However the general trend of the ASE spectra as a function of bias current is confirmed by the model as is the wide optical bandwidth.

The output polarization dependent ASE spectral density (W/Hz) at E_k is given by

$$\sigma_{\rm TE/TM,k} = \frac{hE_k}{\Delta E} N^+_{\rm TE/TM,k}(z = L). \tag{18}$$

The polarization dependent noise figure spectrum is calculated using [16],

$$NF_{\rm TE/TM,k} = 10 \log_{10} \left(\frac{2\sigma_{\rm TE/TM,k}}{E_k G_{\rm TE/TM,k}} \right) \text{dB} \tag{19}$$

where $G_{\rm TE/TM,k}$ is the TE or TM signal gain spectrum. The bias current dependency of the TE small-signal gain and noise figure at 1.46 μm are shown in Fig. 7, showing good agreement with experiment.

It is challenging to obtain good matching between experiment and simulation over a wide range of currents and wavelength. This is because QW bandstructure and material gain calculations are more complicated than for bulk material as there are comparatively many more unknown or difficult to measure model parameters. Furthermore, it is also challenging to predict the mutual interaction of the different order confined energy levels, which clearly appear in the lower wavelength region as the injected current is increased. The TE gain spectrum has clearly two peaks at 1.57 and 1.46 μm, corresponding to three different transitions. The low energy peak at 1.55 μm is due to the transitions between the first confined electron level and both first heavy and light hole states, which, given the QW width and the low strain value, are almost degenerated. The higher energy peak at 1.46 μm is due to the transition between the second confined electron level and the second heavy hole level.

The model can be used to determine the SOA carrier density and photon density distributions and the principle carrier recombination mechanisms. When the input signal power is

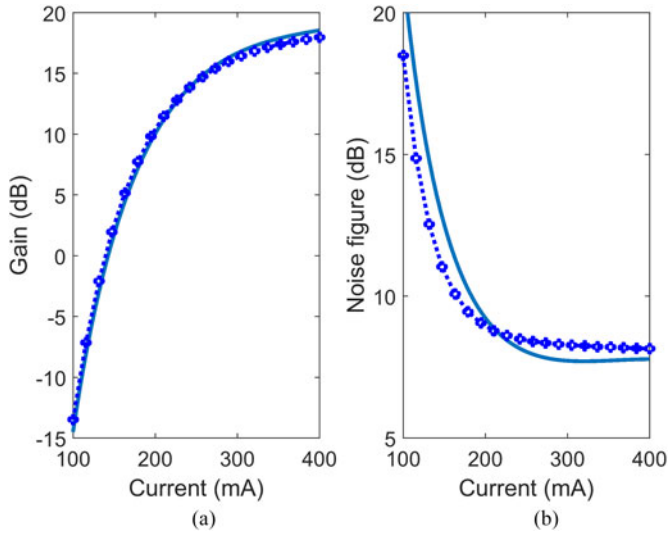

Fig. 7. Experimental (–o) and simulated (−): TE (a) small-signal gain and (b) noise figure versus bias current at 1.46 μm.

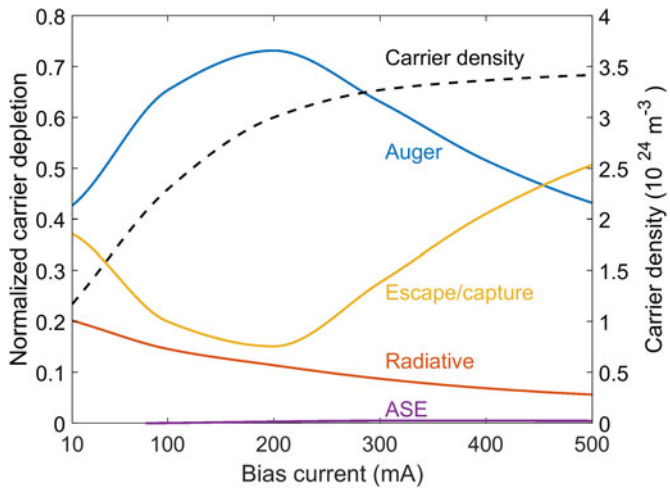

Fig. 8. Bias current dependency of the relative contributions of the depletion terms on the RHS of (13) to the overall carrier density depletion and the spatially independent carrier density.

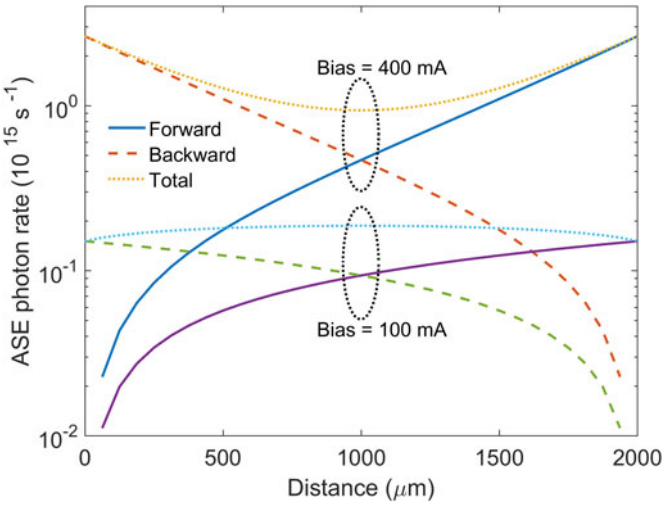

Fig. 9. Spatial dependency of the total ASE for two values of bias current for no input signal.

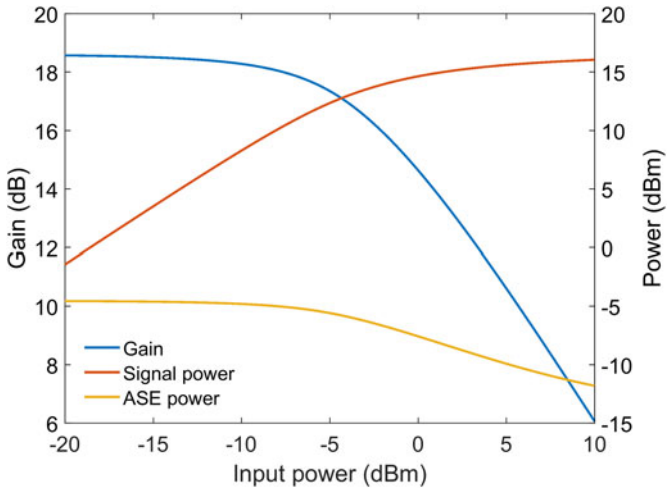

Fig. 10. Simulated TE gain, signal and total ASE powers for bias current of 400 mA and wavelength of 1.46 μm.

negligible, simulations show that the carrier depletion due to the signal and ASE is very small and consequently the well carrier density has almost no spatial dependence. The bias current dependency of the spatially independent carrier density and the contributions of the various terms in (15) normalized to the pump term $I/(eN_wL_wWL)$, to (14) are shown in Fig. 8. For bias currents greater than 150 mA, where the peak gain exceeds 0 dB, the principle recombination processes are Auger and carrier escape/capture processes, the latter becoming increasing prominent at high bias currents as the carrier density approaches n_0, indicating the importance of barrier effects. The spatial dependency of the ASE is shown in Fig. 9 for low and high values of the bias current, showing the expected symmetry. At low bias currents, where the peak gain is less than 0 dB, the total ASE is a maximum at the center of the SOA, whereas at bias currents where the peak gain is greater than 0 dB the total ASE attains its maximum value at both ends.

It is also of interest to model the SOA saturation characteristics. Simulated TE gain, signal power and ASE power versus input power characteristics are shown in Fig. 10. Carrier density distributions are shown in Fig. 11 for a bias current of 400 mA, which corresponds to an unsaturated TE gain of 19 dB at 1.46 μm. It can be clearly seen that as the input signal power increases the carrier density distribution becomes more asymmetrical due to the increasing dominance of the forward propagating signal. Fig. 12(a) shows the spatial distributions of the signal and ASE photon rates for an input TE signal power of −10 dBm corresponding to a low degree of saturation. The spatial dependency of the carrier density and the contributions of the various terms on the Right Hand Side (RHS) of (14) normalized to the pump term $I/(eN_wL_wWL)$, are shown in Fig. 12(b). The carrier density is relatively uniform. As the

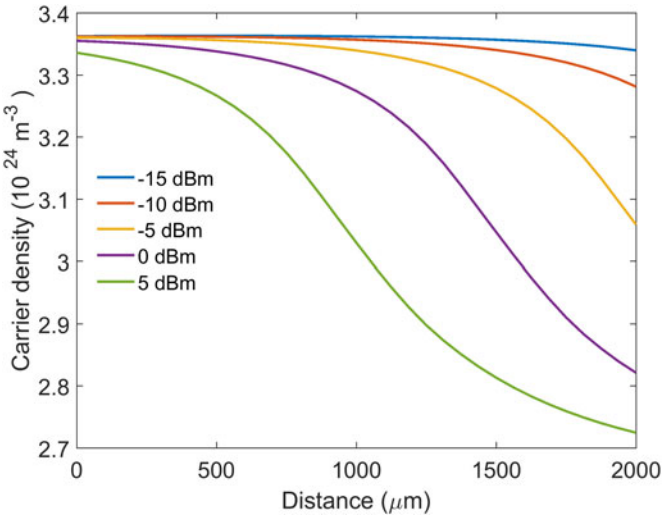

Fig. 11. Simulated carrier density distribution for various TE signal input powers. The bias current and wavelength are 400 mA and 1.46 μm respectively.

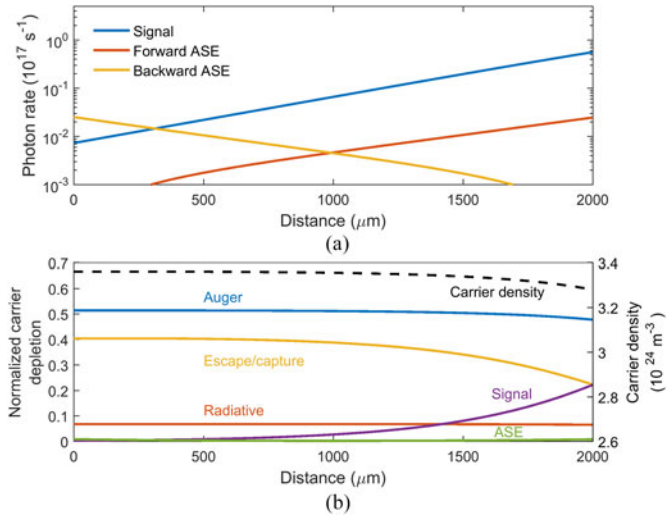

Fig. 12. Spatial dependency (a) signal and ASE photon rates and (b) relative contribution of the depletion terms on the RHS of (14) to the overall carrier density depletion. The bias current, TE polarized signal wavelength and power are 400 mA, 1.46 μm and –10 dBm respectively.

signal becomes amplified as it propagates through the SOA, its contribution to carrier depletion increases mainly at the expense of the net escape/capture processes; the Auger contribution is not significantly affected.

Fig. 13(a) shows the spatial distributions of the signal and ASE photon rates for an input TE signal power of 5 dBm corresponding to a high degree of saturation (the gain has reduced to 10.5 from 19 dB) and the signal power greatly exceeds the ASE. As can be seen in Fig. 13(b) the carrier density distribution becomes asymmetric and the amplified signal becomes the dominant recombination process especially near the SOA output. Escape/capture processes could probably be reduced by using higher band gap energy barrier materials such as

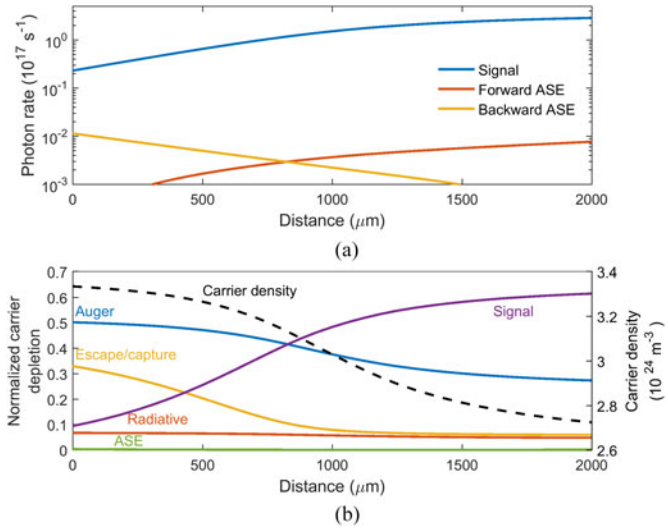

Fig. 13. Spatial dependency of (a) signal and ASE photon rates and (b) relative contribution of the depletion terms on the RHS of (14) to the overall carrier density depletion. The bias current, TE polarized signal wavelength and power are 400 mA, 1.46 μm and 5 dBm respectively.

$In_{0.906}Ga_{0.094}As_{0.207}P_{0.793}$ to ensure efficient carrier confinement in the quantum-wells [2].

There are very few studies in the literature that model MQW-SOA steady-state characteristics spanning detailed wideband calculations of the material gain, additive spontaneous emission and recombination and use this information in accurate traveling-wave equations for the amplified signal and ASE that are solved along with a carrier density rate equation, from which the optical power and inhomogeneous carrier density spatial distributions can be predicted. Prediction of the latter is of particular importance in SOAs [17]. The model does not include the effects of Auger related carrier heating, which can impact on the shape of the ASE spectra particularly at high carrier densities [18]. In including carrier heating effects should lead to improved model accuracy. The device temperature might be higher than that assumed in our model and the carrier temperature is probably higher than the lattice temperature. This explains qualitatively why the experimental ASE drops faster than the theoretical one in the high energy range.

IV. Conclusion

A wideband steady-state model of a strained MQW-SOA has been described, which uses an asymmetric broadening function in the material gain and additive spontaneous emission calculations. Doing so, we obtain good agreement with experimental polarization resolved ASE spectra. The model and parameter extraction leads to the estimation of meaningful model parameters that characterize difficult to model processes including intraband gain broadening, bandgap shrinkage, Auger recombination, carrier escape/capture and IVBA. Dominant recombination mechanisms for low input signal power are linked to Auger recombination as well as net escape/capture processes; the latter is particularly important when high carrier densities

are present due to poor carrier confinement effects. However this latter could be improved by using higher barrier materials. At high input signal powers the carrier depletion induced by the amplified signal becomes important and primarily competes with Auger and escape/capture processes.

REFERENCES

[1] M. A. Newkirk, B. I. Miller, U. Koren, M. G. Young, M. Chien, R. M. Jopson, and C. Burrus, "1.5 μm MQW semiconductor optical amplifier with tensile and compressively strained wells for polarization independent gain," *IEEE Photon. Technol. Lett.*, vol. 10, pp. 553–556, 1993.

[2] H. Carrère, V. G. Truong, X. Marie, R. Brenot, G. De Valicourt, F. Lelarge and T. Amand, "Large optical bandwidth and polarization insensitive semiconductor optical amplifiers using strained InGaAsP quantum wells," *Appl. Phys. Lett.*, vol. 97, 2010, Art. no. 121101.

[3] R. Eppenga, M. F. H. Schuurmans, and S. Colak, "New $k{\cdot}p$ theory for GaAs/$Ga_{1-x}A1_xAs$-type quantum wells," *Phys. Rev. B*, vol. 36, no. 3, pp. 1554–1564, 1987.

[4] D. Ahn and S. L. Chuang, "Optical gain and gain suppression of quantum-well lasers with valence band mixing," *IEEE J. Quantum Electron.*, vol. 26, no. 1, pp. 13–24, Jan. 1990.

[5] X. Marie, J. Barrau, T. Amand, H. Carrère, A. Arnoult, C. Fontaine, and E. Bedel-Pereira, "Band structure and optical gain in InGaAsN/GaAs and InGaAsN/GaAsN quantum wells," *IEE Proc.-Optoelectron.*, vol. 150, no. 1, pp. 25–27, Feb. 2003.

[6] H. Carrère, X. Marie, J. Barrau, T. Amand, S. Ben Bouzid, V. Sallet, and J.-C. Harmand, "Band structure calculations for dilute nitride quantum wells under compressive or tensile strain," *J. Phys. Condens. Matter*, vol. 16, no. 31, pp. S3215–S3227, 2004.

[7] S. L. Chuang, *Physics of Optoelectronic Devices*. New York, NY, USA: Wiley, 1995.

[8] P. M. Enders, "Enhancement and spectral shift of optical gain in semiconductors from non-Markovian intraband relaxation," *IEEE J. Quantum Electron.*, vol. 33, no. 4, pp. 580–588, Apr. 1997.

[9] A. L. Stancik and E. B. Brauns, "A simple asymmetric lineshape for fitting infrared absorption spectra," *Vibrational Spectroscopy*, vol. 47, no. 1, pp. 66–69, 2008.

[10] M. Asada, "Intraband relaxation time in quantum-well lasers," *IEEE J. Quantum Electron.*, vol. 25, no. 9, pp. 2019–2026, Sep. 1989.

[11] M. J. Connelly, "Wide-band steady-state numerical model and parameter extraction of a tensile-strained bulk semiconductor optical amplifier," *IEEE J. Quantum Electron.*, vol. 43, no. 1, pp. 47–56, Jan. 2007.

[12] A. Afzali-Kushaa and G. I. Haddad, "Effects of biaxial strain on the intervalence band absorption spectra of InGaAs/InP systems," *J. Appl. Phys.*, vol. 77, no. 12, pp. 6549–6556, 1995.

[13] G. Lenz, E. P. Ippen, J. M. Wiesenfeld, M. A. Newkirk, and U. Koren, "Femtosecond dynamics of the nonlinear anisotropy in polarization insensitive semiconductor optical amplifiers," *Appl. Phys. Lett.*, vol. 68, no. 21, pp. 2933–2935, 1996.

[14] M. G. Cara, L. Occhi, and S. Balle, "Modeling and measurement of the wavelength-dependent output properties of quantum-well optical amplifiers: Effects of a carrier-dependent escape time," *IEEE J. Sel. Topics Quantum Electron.*, vol. 9, no. 3, pp. 783–787, May/Jun. 2003.

[15] M. J. Connelly, "Wideband semiconductor optical amplifier steady-state numerical model," *IEEE J. Quantum Electron.*, vol. 37, no. 3, pp. 439–447, Mar. 2001.

[16] D. M. Baney, P. Gallion, and R. S. Tucker, "Theory and measurement techniques for the noise figure of optical amplifiers," *Opt. Fiber Technol.*, vol. 6, pp. 122–154, 2000.

[17] J.-N. Fehr, M.-A. Dupertuis, T. P. Hessler, L. Kappei, D. Marti, P. E. Selbmann, B. Deveaud, J. Pleumeekers, J.-Y. Emery, and B. Dagens, "Direct observation of longitudinal spatial hole burning in semiconductor optical amplifiers with injection," *Appl. Phys. Lett.*, vol. 78, pp. 4079–4081, 2001.

[18] J.-N. Fehr, M.-A. Dupertuis, T. P. Hessler, L. Kappei, D. Marti, F. Salleras, M. S. Nomura, B. Deveaud, J. Pleumeekers, J.-Y. Emery, and B. Dagens, "Hot phonons and Auger related carrier heating in semiconductor optical amplifiers," *IEEE J. Quantum Electron.*, vol. 38, no. 6, pp. 674–681, Jun. 2002.

Authors' biographies not available at the time of publication.